applied sciences

MDPI

Article

Experimental Demonstration of a Multichannel Elastic Wave Filter in a Phononic Crystal Slab

Mohd Syafiq Faiz [1,2], Mahmoud Addouche [1], Ahmad Rifqi Md. Zain [2,*,†], Kim S. Siow [2], Amar Chaalane [1] and Abdelkrim Khelif [1,*]

[1] Institut FEMTO-ST, CNRS, Université de Bourgogne Franche-Comté 15B Avenue des Montboucons, CEDEX, F-25030 Besançon, France; faiz@femto-st.fr (M.S.F.); mahmoud.addouche@femto-st.fr (M.A.); amar.chaalane@femto-st.fr (A.C.)

[2] Institute of Microengineering and Nanoelectronics (IMEN), Bangi 43600, Selangor, Malaysia; kimsiow@ukm.edu.my

* Correspondence: rifqi@ukm.edu.my (A.R.M.Z.); abdelkrim.khelif@femto-st.fr (A.K.)

† Current address: School of Engineering and Applied Science (SEAS), Harvard University, Cambridge, MA 02138, USA.

Received: 28 May 2020; Accepted: 28 June 2020; Published: 2 July 2020



Abstract: With the aim of selecting particular frequencies of interest and rejecting others, the waveguiding and filtering properties of a two-dimensional phononic crystal slab are investigated in the context of a filtering application. To this end, we designed and manufactured a metallic device that consists of a square lattice of cylindrical pillars mounted on the top of a plate by using 3D printing technology. We respectively explored the theoretical and experimental characteristics of the device by using finite element method, a Micro System Analyzer (MSA) and a scanning laser Doppler vibrometer. The proposed device shows a complete band gap for Lamb wave around 0.3 MHz with a relative band-width of 30%. Tailorable waveguides are realized inside this phononic crystal by inserting several space gaps to achieve a demultiplexing effect through the splitting of an acoustic signal towards three different bandpass frequency channels. The demultiplexing performance has been experimentally demonstrated by achieving rejection levels up to 60 dB. The proposed phononic platform can have a significant impact in signal processing as well as droplet manipulation for biological applications.

Keywords: phononic crystal slabs; phononic waveguiding; lamb waves; wave demultiplexing

1. Introduction

The advent of phononic crystals (PnCs) three decades ago has changed the research paradigm of composite materials and unfolded many potential innovations in acoustic and elastic devices. Basically, PnCs consist of periodic inclusion of different materials with a strong contrast of elastic properties in two (2D) or three-dimensional (3D) arrangement embedded in a matrix background [1]. The introduction of a linear defect in perfect PnCs structures enables the manipulation of waves similarly to photonic crystals such as wave resonators [2], waveguiding phenomena [3], filters [4] and demultiplexing of acoustic/elastic waves [5,6] targeting several applications, among them biophononic devices [7–9]. The number, position and frequency of transmitted pass band waves are tunable either by altering the waveguide aperture [3] or by using heteroradii pillars to create frequency filters [10,11]. The wave propagation can also be directed towards predefined trajectories either via defect lines with the aim of splitting the acoustic beam [12,13] or bending the wave in sharp corners [14–18].

Due to the benefits of finite thickness in confining elastic waves, slab structures have been studied extensively either by using periodic inclusions such as penetrating a hole in the slab or by mounting

periodic pillars on top of the slab [18–21]. These latter are of more interest as they have demonstrated two types of band gaps namely, Bragg and hybridization-induced band gaps. The first type results from wave interferences scattered by inclusions while the second is caused by the hybridation between the discrete frequencies of elastic resonances of pillars and the propagating modes of the slab. For both types, a considerable research effort has been devoted to study the theoretical [22–25], and experimental [26,27] aspects of band gaps and waveguiding phenomena.

In principe, the waveguide can be achieved through the defect paths mechanism, which can be based on either breaking the lattice periodicity by altering the material or changing the geometrical properties of the unit cell [19]. For instance, removing inclusions from perfect crystals is a practical way to break symmetry and to create a line defect inside the band gap region that guides the elastic or acoustic energy [20]. Following the afore-described approach, Vasseur et al. [21] tuned defect distance to manipulate the number of localized modes inside the band-gap. The study has shown that the number of waveguide modes changes monotonically with the width of the defect. In a closely related study, Oudich et al. succeeded in creating one confined mode within the band gap by using different defect sizes [22].

Alternatively, elastic or acoustic waves can be confined through coupled-resonators inserted into a perfect crystal. In particular, the physical and geometrical parameters of a resonator are first tuned to place its discrete frequencies within the band gap range. A number of similar resonators are then placed and coupled through evanescent waves providing a strong confined waveguide. T. T. Wang et al. [28] have experimentally demonstrated this approach of waveguiding based on collective resonances of a chain defect in phononic crystal slab at ultrasonic frequencies.

One of the main applications of these waveguiding functions is demultiplexing, i.e., the process of separating two or more frequencies by introducing perfectly confined defect modes within the band gap. Pennec et al. [29] have reported some theoretical results of a tunable filtering and wave rooting, a type of demultiplexing, using 2D phononic crystals with hollow cylinders. The study was based on waveguiding at selected frequencies inside the band gap by tuning the inner radius of hollow cylinders. The same technique of inner radius tuning was applied more recently by Yabin et al. [30] to control whispering-gallery modes in hollow pillars placed on the top of phononic crystal plate. These theoretical results have led to many fundamental concepts and opens opportunities for potential applications in the area of elastic and acoustic metamaterials. However, experimental studies verifying these fundamental concepts are limited to a few.

This paper analyses, designs and implements a demultiplexing operation across three distinct linear waveguides fabricated on the same planar structure of a pillar-based phononic crystal slab. The three waveguides have been realized by removing one line of pillars. According to the waveguides width variation, the proposed system shows the capability of filtering three frequency regions in the band gap with high level of rejection. The rest of the paper is organized as follows. Section 2, describes the model geometry, the material parameters and the methods of fabrication. The experimental setup and band gap characterization are also introduced in Section 2. Section 3 examines numerically and experimentally the demultiplexing behavior. Conclusions and remarks are given in Section 4.

2. Theory and Experimental Methods

The proposed structure is schematically presented in Figure 1a where a 2D square unit cell is zoomed. The geometrical parameters of the unit cell are as follows: Slab thickness $h = 1\,\text{mm}$, Square lattice parameter $a = 4\,\text{mm}$, height of the pillars $h_p = 4.4\,\text{mm}$, radius of the pillars $r_p = 1.6\,\text{mm}$. The manufactured device is fabricated on the same planar structure using 3D-Printer $ProX300$ via Direct Metal Laser Sintering (DMLS) technology with a resolution of 0.02 mm, as depicted in Figure 1b. The printed metal is an aluminium alloy $AlSi7Mg06$ having Poisson ratio $\nu = 0.33$, Young modulus $E = 76.12\,\text{GPa}$ and mass density $\rho = 2670\,\text{kg}\,\text{m}^{-3}$.

To demonstrate the demultiplexing application, a compact three linear waveguides channels: $W_1 = 1.52\,\text{mm}$, $W_2 = 1.2\,\text{mm}$ and $W_3 = 0.88\,\text{mm}$ were made inside the pillar based phononic crystal, as shown in Figure 1b. Each of these linear waveguides are distanced from one another by 8 rows of pillars inclusion to avoid any cross-talk between the waveguide lines inside the frequency range of the band gap. The total dimension of the structure is $100 \times 172 \times 1\,\text{mm}^3$. The elastic excitation is generated by a piezoelectric ceramic transducer patch made of lead zirconate titanate (Ferroperm PZ27 num. 27303). This PZT patch has a dimension of $15 \times 8 \times 1\,\text{mm}^3$ and acts as a vibration source providing an out-of-plane displacement with a frequency up to 2 MHz. In the frequency range of our interest, the electromechanical coupling factor for thickness mode is equal to 0.47. The patch is bonded on the surface of the device under test by using silver glue, granting a good contact with the plate. Figure 1c illustrates the experimental equipment including a Micro System Analyzer (MSA–500 by *Polytec*) supplied by analog displacement vibration decoder model DD–300 with sensitivity of $50\,\text{nm}\,\text{V}^{-1}$. The latter allows both out and in plane displacement measurements as well as the waveform mapping up to a maximum frequency of 1.5 MHz. The transmission coefficient spectra is estimated by measuring the displacement along both sides of the pillar array. A chirped signal of maximum voltage amplitude of 7 V is supplied between the electrodes of PZT producing mechanical vibration with broadband frequency range extending from 250 kHz to 400 kHz. In order to avoid any surface interaction between the tested device and the *MSA* table, an underneath support that consists of foam prism is used as it is shown in Figure 1d.

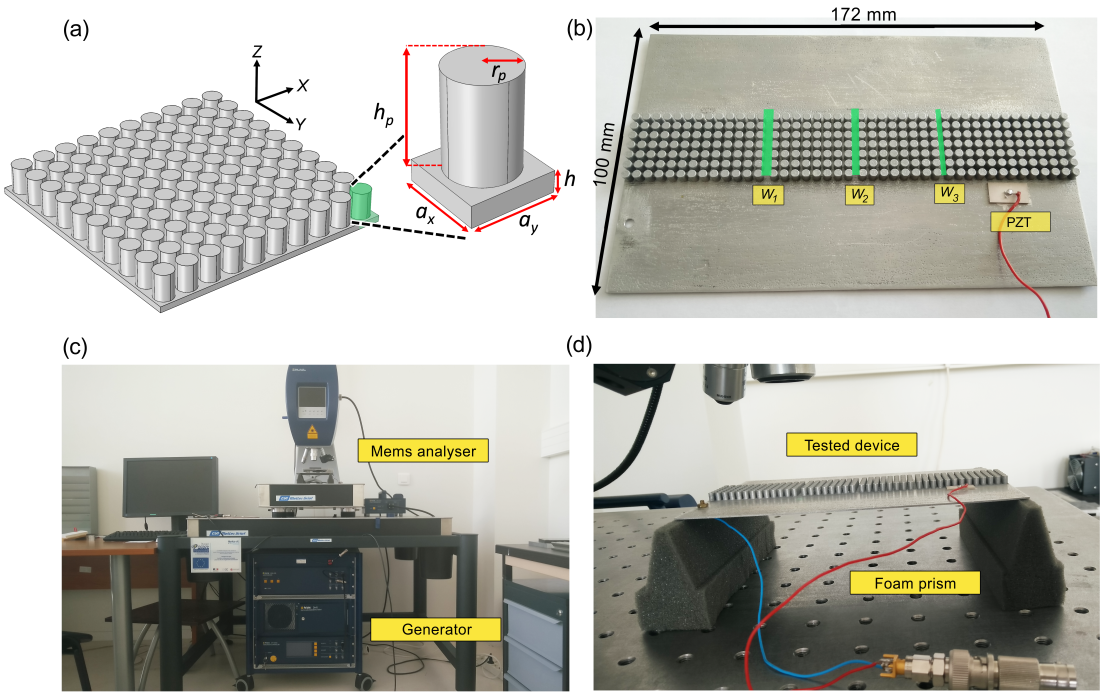


Figure 1. (**a**) unit cell configuration with height of pillar, h_p = 4.4 mm, slab thickness, h = 1 mm, radius, r_p = 1.6 mm, and crystal Lattice, $a_x = a_y$ = 4 mm (**b**) demultiplexer device consists of 3 waveguides channels W_1 = 1.52 mm, W_2 = 1.22 mm and W_3 = 0.88 mm. Soft piezo ceramic (PZ27 by Ferroperm) is glued as source of excitation (**c**) MSA–500 setup to measure transmission spectrum (**d**) foam prism to avoid the device from surface contact with MSA-500 table.

In order to analyze the band diagram and transmission spectrum, we applied Finite Element Method (FEM) to study the band gap effect of equidistant pillar structures in a perfect phononic region. The classical approach based on Bloch–Floquet theorem to represent the boundary conditions of infinite periodicity in x and y-directions are applied to the unitary cell as shown in Figure 1a. Particularly, the periodicity has been applied between the two orthogonal faces in x-direction and also

the two orthogonal faces in y-direction. Whereas, the top and bottom surface in the z-direction have free boundary conditions. The *Bloch-Floquet* approach is considered as follows:

$$u_i(x + a \cdot m, y + a \cdot n, z) = u_i(x, y, z)e^{-\imath a \cdot (k_x m + k_y n)} \tag{1}$$

where k_x and k_y are the components of the *Bloch* wave vectors along the x and y directions. While u_i is the displacement with $i = x$, y and z. The *Bloch* boundary conditions describe the phase relation of propagating wave on the boundaries with Bloch wave vector k. The displacement from one boundary to the other boundary in the directions x and y can therefore be written as: $\mathbf{u}(\mathrm{x}) = e^{-\imath(ak_x m)}\mathbf{u}(x)$ and $\mathbf{u}(\mathrm{y}) = e^{-\imath(ak_y n)}\mathbf{u}(y)$ respectively. The equation for the case of harmonic homogeneous dynamical equilibrium, however, takes the partial derivative as the following forms.

$$\rho\omega^2\mathbf{u} + \nabla[\mathbf{C} \cdot \varepsilon] = 0 \tag{2}$$

where ρ is the mass density, ω is the angular frequency, $\mathbf{u} \in \mathbb{R}^3$ is the displacement vector, $\mathbf{C}$ is the elastic tensor and $\varepsilon = \nabla_{sym}\mathbf{u} = \frac{1}{2}\left[(\nabla\mathbf{u})^T + \nabla\mathbf{u}\right]$ is the strain tensor. Equation (2) combined with *Bloch-Floquet* theorem of Equation (1) have been solved using FEM. The eigenvalues are plotted usually against two wave vector parameters, k_x and k_y, the taken value in the interval $\left[0, \frac{\pi}{a}\right]$ of the first Brillouin zone.

3. Results and Discussions

Before analyzing band diagrams of defect modes, it is necessary to calculate the mode dispersion of the perfect crystal which is considered as a reference for the band structure of defect modes. By changing the value k in the first irreducible Brillouin zone, FEM allows us to solve the eigen-value problem and calculate the band diagram of the phononic crystal. As illustrated in Figure 2a, the band diagram of the perfect crystal shows a complete band gap as well as two partial band gaps for the geometrical parameters listed in the previous section. The two partial band gaps occur at frequency ranges 382 to 405 kHz and 485 to 497 kHz while the complete band gap exists in the range 272 to 347 kHz. This latter appears to be a Bragg band gap, which is due to destructive interferences of the scattering waves from the pillar array. To compare these simulations with experimental results, a transmission through a finite crystal that consists of 7 pillars periods in the direction of incoming wave is shown as a function of frequency in Figure 2b. Numerically, the out-of-plane polarized excitation source is set as the input signal and perfectly matched layers (PML) are incorporated in the direction of outgoing waves to avoid any reflection from the boundaries. On the experimental side, the spatial scanning area of $1.6 \times 1.6\,\mathrm{mm}^2$ (5×5 points spatial grid) on the perfect crystal, i.e., without defect lines, is considered using MSA–500 setting as described earlier. The measurements are represented in the form of Reduced Displacement (RD) according to Equation (3) [31].

$$u_{\mathrm{dB}n} = 20 \cdot log_{10}\left(\frac{1}{N}\sum_{k=1}^{N}\frac{|u_k|}{1\,\mathrm{nm}}\right) \tag{3}$$

where N is the number of measurements made during an integration time of 3.2 ms. The index dBn indicates that the quantity u is expressed in normalized dB scale with reference to one nanometer of displacement (nm).

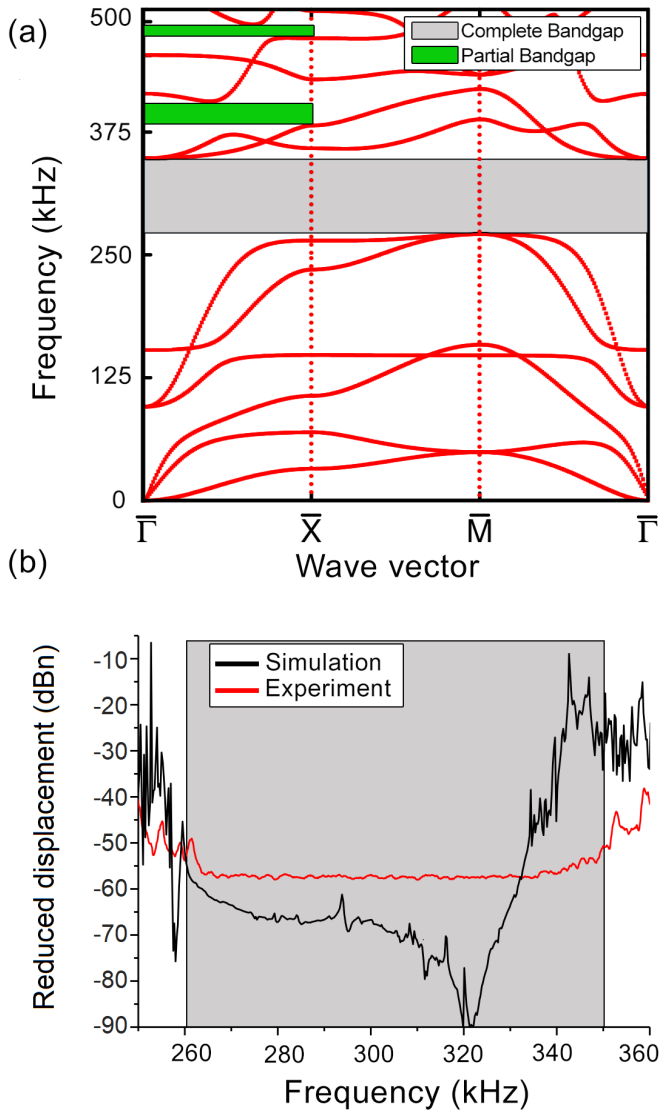


Figure 2. (**a**) Band diagram of unit cell (**b**) simulated (black) and experimental (red) transmission for the band gap between 260 kHz to 347 kHz.

A good agreement between experimental and simulation results shows a pronounced dip in the frequency span between 262 to 347 kHz kHz suggesting the existence of a band gap region as predicted by the dispersion curve. A small discrepancy in the simulated curve showing low frequency shift is justified by the mismatch between the theoretical values of the physical parameters used in the simulation and the experimental values of the printed material that are sensitive to the fabrication conditions.

To show the omnidirectionality of the band gap, we conduct a surface topography measurement with laser Doppler vibrometer (SLDV) *PSV*-5003*DHV*by *Polytec* as depicted in Figure 3a. The instrument has the capability to scan larger surface areas of sizes ranging from a few mm^2 to several cm^2. This capability is sufficient to illustrate a potential situation for the actual wave travelling in devices of larger dimensions. The scanning covered a surface area of $113 \times 56.8\,mm^2$ (proportionate to 97×49 points spatial grid) and took place on the backside surface with no phononic pillar-based structure, Figure 3b. The laser vibrometer is perpendicularly positioned at about 0.8 m distance from the top surface of the device. During the measurement we used only one SLDV head with no noise filter to detect the out-of-plane vibration of the plate surface. A similar procedure is repeated by using a piezoelectric ceramic with an out-of-plane polarized excitation. The same chirped signal

was applied to the piezoelectric transducer ensuring broadband mechanical excitation ranging from 250 to 400 kHz. As noted in Figure 3c, sending a wave within the band gap frequencies, $f = 265$ kHz, results in a total reflection along all directions of the crystal inducing multiple interferences which generate standing waves pattern limited by the white line that marks the crystal boundaries of the device. The effect of this omnidirectionality is corroborated by numerical simulation of a harmonic single source vibrating at the same frequency as shown in Figure 3d. We also observe the same standing waves form as a result of the total reflection from the pillar array. In addition, the numerical simulation shows a strong attenuation of the incident wave along a short distance inside the pillar based phononic crystal.

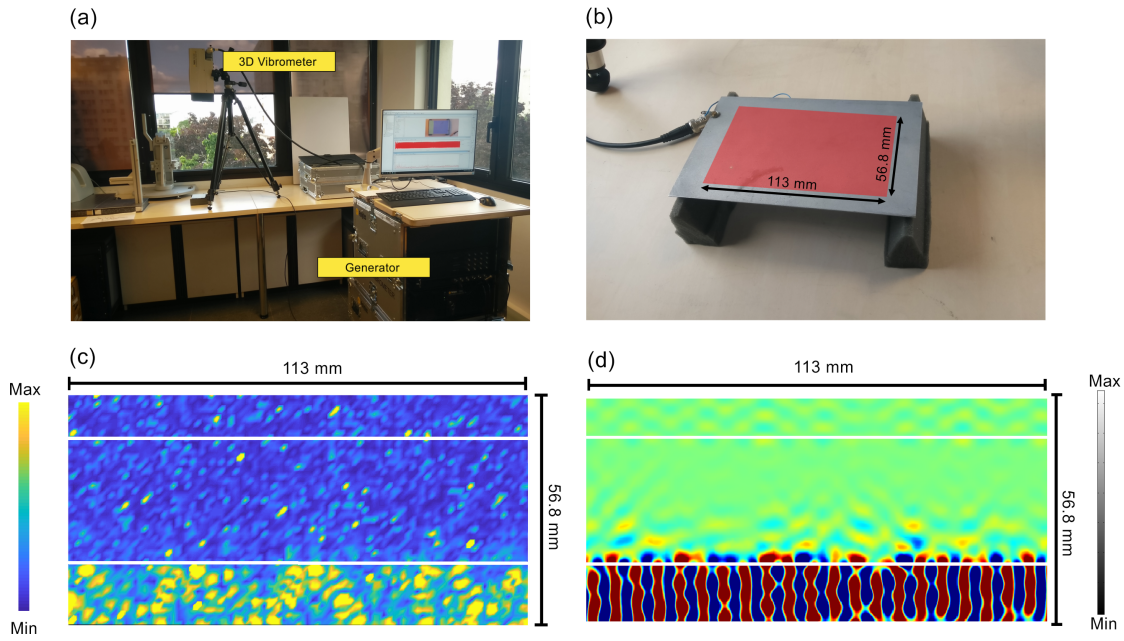


Figure 3. (**a**) PSV-500 set-up to measure the surface cartography displacement for demultiplexer device, (**b**) scanning area (red region) equivalent to 113 mm × 56.8 mm surface dimension, (**c**) experimental surface measurement at the band gap frequency, f = 265 kHz, (**d**) simulated displacement at similar band gap frequency, as (**c**). The white lines mark the boundaries of the pillar based phononic crystal in both (**d**) and (**c**).

Different defects inside the perfect crystal are introduced by inserting a space gap between two rows of pillars in the wave propagating direction. The defect width ensures the presence of multiple waveguide modes inside the band gap. The band diagram of the waveguiding prediction is based on supercell technique. Figure 4a illustrates the 1×7 supercell with defect width W_g that has been used to calculate dispersion relations and the eigenvectors of the defect modes. This technique assumes a periodic boundary condition, with phase varying, along x direction and periodic continuity, without phase change, in y direction. The 8 rows of pillars that separate each of these linear waveguides, along y axis, are sufficient to avoid any interaction between the waveguide lines in the frequency band gap region. The geometry variables of defect-containing structures, i.e., lattice parameters, a, height, h_p and radius, r_p of pillar are maintained as perfect crystals to ensure a similar frequency gap limit. To run numerical simulation for guiding effect, three defects widths $W_1 = 1.52$ mm, $W_2 = 1.2$ mm and $W_3 = 0.88$ mm are set up. These waveguide apertures are carefully designed to cover a wide range of frequencies within the band gap and to ensure a selective transmission in each path of the waveguides.

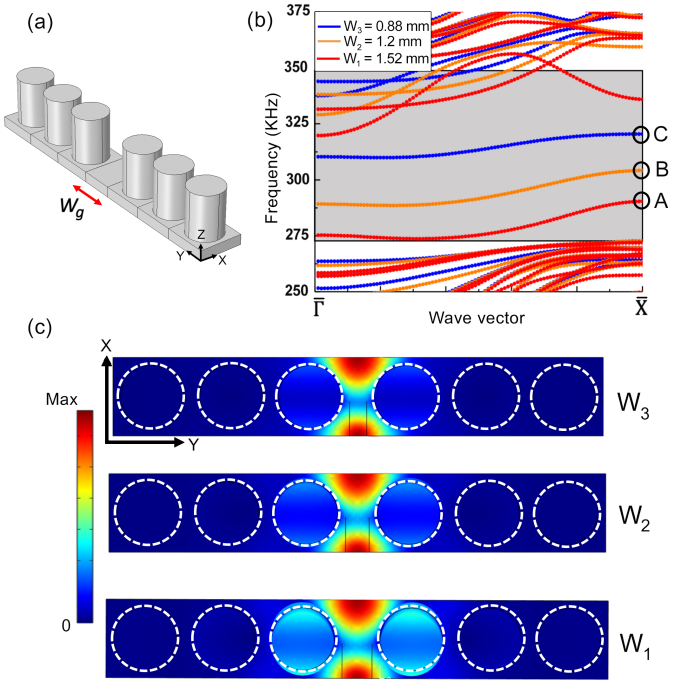


Figure 4. (**a**) Supercell technique to measure three waveguide dispersion curves. W_g is the defect distance with W_1 = 1.52 mm, W_2 = 1.22, W_3 = 0.88 mm. (**b**) Dispersion curve for W_1 = 1.52 mm (red), W_2 = 1.22 (orange), W_3 = 0.88 mm (blue). The grey area is the band gap region that ranges from 274 kHz to 350 kHz. (**c**) The out-of plane displacement profile for waveguides, W_1 (bottom), W_2 (middle) and W_3 (top). The dotted-circle indicate the pillar structures.

The numerical study summarized in Figure 4b reveals several pass bands that do not exist in native perfect crystal structures due to the defect modes associated with the different waveguide widths. Basically, the three different waveguide thicknesses insert three branches at different cutoff frequencies inside the band gap, as depicted in Figure 4b with marks A, B, C. It covers range of frequencies $f_{W_1} = 275{-}288$ kHz, $f_{W_2} = 288{-}303$ kHz and $f_{W_3} = 310{-}320$ kHz that represents waveguides W_1 , W_2 and W_3. The position and frequencies of these pass bands are adjustable as a function of the waveguides' widths. At higher frequencies, beyond the C band, numerous transmitting bands occur inside the band gap, which are related to new modes or to the folding back of the waveguide bands that appear at low frequencies of the band gap. This folding is due to the pillar edges periodicity of the waveguide line. The transmitting bands close to the band gap upper limit are not used in the demultiplexing operation for two reasons: (1) the pass band has interaction with the bulk modes, i.e., Lamb modes, which induce a radiation in other directions of propagation (2) each pass band crisscrossing with one another and create a weakly interaction between transmitting bands. Thus, these two conditions reduce the energy confinement within the waveguide and therefore have been ignored in our transmission band selection.

To illustrate the transmitting wave inside the waveguides, we calculate the out-of-plane displacement at the limit of the first Brillouin zone around X point in Figure 4c, three consecutive frequencies $f_A = 288$ kHz, $f_B = 303$ kHz and $f_C = 320$ kHz, which respectively, present the waveguide W_1 (bottom), W_2 (middle) and W_3 (top) are calculated. The out-of-plane displacement clearly shows a spatial confinement of the energy inside the defect for three waveguides cases and only interacts weakly with the neighboring pillars. The theoretical results present important characteristics for the possibility of tunable elastic waves filter in slab structure by changing the defect distance between two neighboring pillars. In addition, the strong attenuation in lateral direction (along y axis) shows the vanishment of the Lamb wave magnitude after three periods. Consequently, a minimum

of seven periods between two waveguide lines ensures there is no interaction in the lateral side of the waveguide lines.

To verify experimentally the feasibility of our waveguides as a filter, an actual device that consists of three line-defect waveguides as described by Section 2, is manufactured. To measure the transmission coefficient experimentally, a similar setup to the one reported in the Section 2 with $MSA500$ is used where the spot of laser interferometer is focused at the end of each waveguide line. The scanning area consists of a square surface of $4 \times 4\,\mathrm{mm}^2$ divided into 16 measurement nodes. For each frequency, and for each waveguide, an average of the 16 nodes of the out-of-plane displacement measurement is calculated and reported in Figure 5. As predicted, the experimental transmission coefficient reveals three bands inside the band gap. The device acts as a frequency filter in three frequency ranges of $f_{W_1} = 274 - 287\,\mathrm{kHz}$ (red curve), $f_{W_2} = 285 - 300\,\mathrm{kHz}$ (orange curve) and $f_{W_3} = 301 - 315\,\mathrm{kHz}$ (blue curve). It is also noticed that the bands W_1 and W_2 are completely separated, i.e., without crossing over. For instance, the transmission magnitude of W_2 drops immediately at frequency $f = 302\,\mathrm{kHz}$ (orange curve) while at the same time, a notable transmission peak occurs at frequency $f = 305\,\mathrm{kHz}$ which represents W_3 channel defects (Blue curve). On the other hand, the bands W_3 and W_2 have a common narrow band that extends from 280 to 287 kHz. The theoretical transmission shown in Figure 5b has a similar noticeable peak and dip transmission comparable to the experimental data. Finally, an input signal that covers the bandwith of the band gap will be transmitted separately along W_1, W_2 and W_3 according to frequency range of each waveguide. This shows the capability of the device to act as a wave demultiplexer.

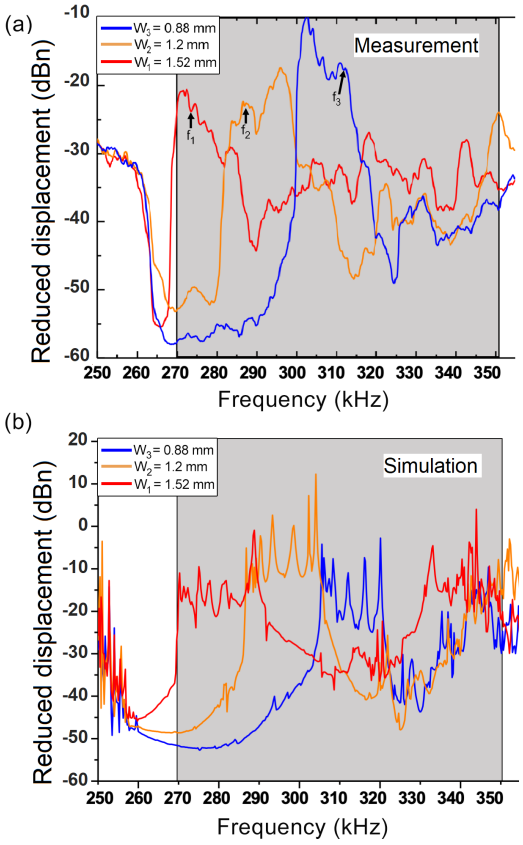


Figure 5. (**a**) Experimental and (**b**) simulated transmission spectra for three waveguide channels W_1, W_2 ,W_3. The grey area marks the region for band gap.

To demonstrate the separation of the Lamb wave through the filter device, a displacement field measurement based on scanning laser Doppler vibrometer (SLDV) is realized as shown in Figure 6. The measurement procedure is similar to the method described in Section 2. Figure 6

corresponds to the theoretical and experimental data of the out-of-plane displacement for the wave propagating through the demultiplexing structure. In particular, a frequency swept from 250 kHz to 400 kHz is supplied to every waveguide entrance to study their response. Figure 6a shows that the waveguides provide filtering frequencies and incident waves routed into one waveguide that belongs to W_3 channels with frequency at 275 kHz. A noticeable wave attenuation over a wide range of frequencies is successfully demonstrated in the channels W_2 and W_1, which respectively have filtering frequencies $f_{W_2} = 288 - 303$ kHz and $f_{W_1} = 275 - 288$ kHz. Similarly, in Figure 6b,c, both experiments and simulations show a similar selectivity profile. In Figure 6b, the incoming waves with $f_2 = 288.4$ kHz were totally attenuated except in the middle channel for W_2. The same filtering phenomena is observed at the frequency $f_3 = 314$ kHz for W_1 channel as illustrated in Figure 6c.

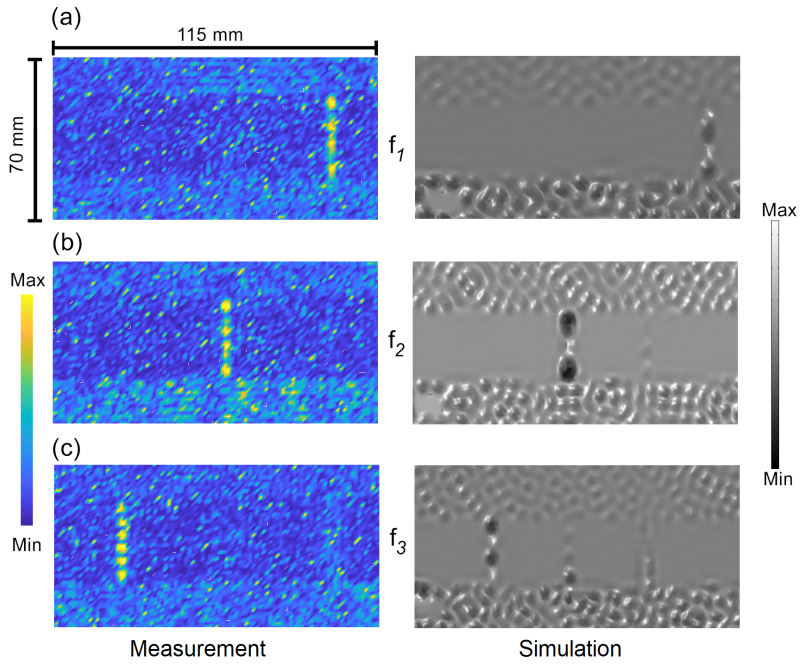


Figure 6. Comparison between simulation and experiment for surface cartography displacement in z-direction for (**a**) W_3 = 0.88 mm at 274 kHz (**b**) W_2 = 1.22 mm at 288.4 kHz (c) W_1 = 1.52 mm at 314 kHz.

4. Conclusions

In summary, we have demonstrated an elastic multichannel filter for Lamb waves, which used three different phononic waveguide defects inside a square array of cylindrical pillars mounted on the top of a plate. The device was fabricated using 3D metal printers based on aluminium alloy, *AlSi7Mg*06. The band gap and the selective waveguiding properties have been experimentally demonstrated using a scanning laser Doppler vibrometer (PSV–500 3D HV) to image the out-of-plane displacement field and using a micro system analyzer (MSA–500) to measure the transmission of the acoustic waves inside each of the three waveguiding channels. The device shows a complete band gap for *Lamb* wave gap centred at 300 kHz with a relative band-width of 30%. Tailorable waveguides are realized inside this phononic crystal by inserting several space gaps between pillars allowing the transmission of three frequency bands of 280 kHz ± 7%, 293 kHz ± 8% and 308 kHz ± 7%. The splitting of the acoustic signal to corresponding channels was achieved with a high rejection level of 60 dB. Each waveguide appears to transmit the wave exclusively to their cuttoff frequencies without a significant loss to other waveguide routes, signifying the demultiplexing capabilities of the proposed design, which can be used in droplet manipulation for biological applications.

Author Contributions: Conceptualization, M.A. and A.K.; investigation, M.A.; resources, K.S.S.; writing—original draft preparation, M.S.F.; writing—review and editing, A.R.M.Z. and A.C.; supervision, A.K.; All authors have read and agreed to the published version of the manuscript.

Funding: This work was supported by the Publication Acceleration Fund HICOE AKU254, Ministry of Higher Education of Malaysia and Double-Degree PHD scholarship from French Embassy in Malaysia.

Acknowledgments: This work was supported by the EIPHI Graduate School (contract "ANR-17-EURE-0002"), French ambassy in Malysia. We thank *Polytech* staff for assistance with the optical measurment technique and Hamza Baali for comments that greatly improved the manuscript.

Conflicts of Interest: The authors declare no conflict of interest.

References

1. Deymier, P.A. *Acoustic Metamaterials and Phononic Crystals*; Springer Science & Business Media: Berlin, Germany, 2013; Volume 173.
2. Mohammadi, S.; Eftekhar, A.A.; Hunt, W.D.; Adibi, A. High-Q micromechanical resonators in a two-dimensional phononic crystal slab. *Appl. Phys. Lett.* **2009**, *94*, 051906. [CrossRef]
3. Khelif, A.; Djafari-Rouhani, B.; Vasseur, J.; Deymier, P.A. Transmission and dispersion relations of perfect and defect-containing waveguide structures in phononic band gap materials. *Phys. Rev. B* **2003**, *68*, 024302. [CrossRef]
4. Rostami-Dogolsara, B.; Moravvej-Farshi, M.K.; Nazari, F. Acoustic add-drop filters based on phononic crystal ring resonators. *Phys. Rev. B* **2016**, *93*, 014304. [CrossRef]
5. Hsu, J.C. Switchable frequency gaps in piezoelectric phononic crystal slabs. *Jpn. J. Appl. Phys.* **2012**, *51*, 07GA04. [CrossRef]
6. Rostami-Dogolsara, B.; Moravvej-Farshi, M.K.; Nazari, F. Designing Switchable Phononic Crystal-Based Acoustic Demultiplexer. *IEEE Trans. Ultrason. Ferroelectr. Freq. Control.* **2016**, *63*, 1468–1473. [CrossRef]
7. Bourquin, Y.; Wilson, R.; Zhang, Y.; Reboud, J.; Cooper, J.M. Phononic Crystals for Shaping Fluids. *Adv. Mater.* **2011**, *23*, 1458–1462. [CrossRef]
8. Wilson, R.; Reboud, J.; Bourquin, Y.; Neale, S.L.; Zhang, Y.; Cooper, J.M. Phononic crystal structures for acoustically driven microfluidic manipulations. *Lab Chip* **2011**. [CrossRef]
9. Hsu, J.-C.; Lin, Y.D. Microparticle concentration and separation inside a droplet using phononic-crystal scattered standing surface acoustic waves. *Sens. Actuators A Phys.* **2019**, *300*. [CrossRef]
10. Taleb, F.; Darbari, S. Tunable Locally Resonant Surface-Acoustic-Waveguiding Behavior by Acoustoelectric Interaction in Zn O-Based Phononic Crystal. *Phys. Rev. Appl.* **2019**, *11*, 024030. [CrossRef]
11. Guo, Y.; Schubert, M.; Dekorsy, T. Finite element analysis of surface modes in phononic crystal waveguides. *J. Appl. Phys.* **2016**, *119*, 124302. [CrossRef]
12. Li, J.; Wu, F.; Zhong, H.; Yao, Y.; Zhang, X. Acoustic beam splitting in two-dimensional phononic crystals using self-collimation effect. *J. Appl. Phys.* **2015**, *118*, 144903. [CrossRef]
13. Guo, Y.; Brick, D.; Grossmann, M.; Hettich, M.; Dekorsy, T. Acoustic beam splitting at low GHz frequencies in a defect-free phononic crystal. *Appl. Phys. Lett.* **2017**, *110*. [CrossRef]
14. Miyashita, T.; Inoue, C. Numerical investigations of transmission and waveguide properties of sonic crystals by finite-difference time-domain method. *Jpn. J. Appl. Phys.* **2001**, *40*, 3488. [CrossRef]
15. Addouche, M.; Al-Lethawe, M.A.; Elayouch, A.; Khelif, A. Subwavelength waveguiding of surface phonons in pillars-based phononic crystal. *AIP Adv.* **2014**, *4*, 124303. [CrossRef]
16. Celli, P.; Gonella, S. Manipulating waves with LEGO® bricks: A versatile experimental platform for metamaterial architectures. *Appl. Phys. Lett.* **2015**, *107*, 081901. [CrossRef]
17. Sun, J.H.; Wu, T.T. Propagation of acoustic waves in phononic-crystal plates and waveguides using a finite-difference time-domain method. *Phys. Rev. B* **2007**, *76*, 104304. [CrossRef]
18. Pennec, Y.; Djafari-Rouhani, B.; Larabi, H.; Vasseur, J.; Hladky-Hennion, A. Low-frequency gaps in a phononic crystal constituted of cylindrical dots deposited on a thin homogeneous plate. *Phys. Rev. B* **2008**, *78*, 104105. [CrossRef]
19. Wu, T.C.; Wu, T.T.; Hsu, J.C. Waveguiding and frequency selection of Lamb waves in a plate with a periodic stubbed surface. *Phys. Rev. B* **2009**, *79*, 104306. [CrossRef]

20. Vasseur, J.; Hladky-Hennion, A.C.; Djafari-Rouhani, B.; Duval, F.; Dubus, B.; Pennec, Y.; Deymier, P.A. Waveguiding in two-dimensional piezoelectric phononic crystal plates. *J. Appl. Phys.* **2007**, *101*, 114904. [CrossRef]
21. Vasseur, J.; Deymier, P.A.; Djafari-Rouhani, B.; Pennec, Y.; Hladky-Hennion, A. Absolute forbidden bands and waveguiding in two-dimensional phononic crystal plates. *Phys. Rev. B* **2008**, *77*, 085415. [CrossRef]
22. Oudich, M.; Assouar, M.B.; Hou, Z. Propagation of acoustic waves and waveguiding in a two-dimensional locally resonant phononic crystal plate. *Appl. Phys. Lett.* **2010**, *97*, 193503. [CrossRef]
23. Pourabolghasem, R.; Khelif, A.; Mohammadi, S.; Eftekhar, A.A.; Adibi, A. Physics of band-gap formation and its evolution in the pillar-based phononic crystal structures. *J. Appl. Phys.* **2014**, *116*, 013514. [CrossRef]
24. Oudich, M.; Li, Y.; Assouar, B.M.; Hou, Z. A sonic band gap based on the locally resonant phononic plates with stubs. *New J. Phys.* **2010**, *12*, 083049. [CrossRef]
25. Badreddine Assouar, M.; Oudich, M. Enlargement of a locally resonant sonic band gap by using double-sides stubbed phononic plates. *Appl. Phys. Lett.* **2012**, *100*, 123506. [CrossRef]
26. Oudich, M.; Senesi, M.; Assouar, M.B.; Ruzenne, M.; Sun, J.H.; Vincent, B.; Hou, Z.; Wu, T.T. Experimental evidence of locally resonant sonic band gap in two-dimensional phononic stubbed plates. *Phys. Rev. B* **2011**, *84*, 165136. [CrossRef]
27. Zhang, S.; Hui Wu, J.; Hu, Z. Low-frequency locally resonant band-gaps in phononic crystal plates with periodic spiral resonators. *J. Appl. Phys.* **2013**, *113*, 163511. [CrossRef]
28. Wang, T.; Bargiel, S.; Lardet-Vieudrin, F.; Wang, Y.F.; Wang, Y.S.; Laude, V. Collective Resonances of a Chain of Coupled Phononic Microresonators. *Phys. Rev. Appl.* **2020**, *13*, 014022. [CrossRef]
29. Pennec, Y.; Djafari-Rouhani, B.; Vasseur, J.; Khelif, A.; Deymier, P.A. Tunable filtering and demultiplexing in phononic crystals with hollow cylinders. *Phys. Rev. E* **2004**, *69*, 046608. [CrossRef]
30. Jin, Y.; Fernez, N.; Pennec, Y.; Bonello, B.; Moiseyenko, R.P.; Hémon, S.; Pan, Y.; Djafari-Rouhani, B. Tunable waveguide and cavity in a phononic crystal plate by controlling whispering-gallery modes in hollow pillars. *Phys. Rev. B* **2016**, *93*, 054109. [CrossRef]
31. Coffy, E.; Euphrasie, S.; Addouche, M.; Vairac, P.; Khelif, A. Evidence of a broadband gap in a phononic crystal strip. *Ultrasonics* **2017**, *78*, 51–56. [CrossRef]



© 2020 by the authors. Licensee MDPI, Basel, Switzerland. This article is an open access article distributed under the terms and conditions of the Creative Commons Attribution (CC BY) license (http://creativecommons.org/licenses/by/4.0/).